



Magellanic System Stars Identified in SMACS J0723.3-7327 James Webb Space Telescope Early Release Observations Images

Jake Summers¹ , Rogier A. Windhorst¹ , Seth H. Cohen¹ , Rolf A. Jansen¹ , Timothy Carleton¹ , Patrick S. Kamienieski¹ ,
Benne W. Holwerda² , Christopher J. Conselice³ , Nathan J. Adams³ , Brenda L. Frye⁴ , Jose M. Diego⁵ ,
Christopher N. A. Willmer⁴ , Rafael Ortiz, III¹ , Cheng Cheng⁶ , Alex Pigarelli¹ , Aaron Robotham⁷ ,
Jordan C. J. D'Silva^{7,8} , Scott Tompkins^{1,7} , Simon P. Driver⁷ , Haojing Yan⁹ , Dan Coe¹⁰ , Norman Grogin¹¹ ,
Anton M. Koekemoer¹¹ , Madeline A. Marshall^{8,12} , Nor Pirzkal¹¹ , and Russell E. Ryan, Jr.¹¹ 

¹ School of Earth and Space Exploration, Arizona State University, Tempe, AZ 85287-1404, USA; jssumme1@asu.edu

² Department of Physics and Astronomy, University of Louisville, Louisville, KY 40292, USA

³ Jodrell Bank Centre for Astrophysics, Alan Turing Building, University of Manchester, Oxford Road, Manchester M13 9PL, UK

⁴ Steward Observatory, University of Arizona, 933 N Cherry Ave, Tucson, AZ 85721-0009, USA

⁵ Instituto de Física de Cantabria (CSIC-UC), Avenida. Los Castros s/n. E-39005 Santander, Spain

⁶ Chinese Academy of Sciences, National Astronomical Observatories, CAS, Beijing 100101, People's Republic of China

⁷ International Centre for Radio Astronomy Research (ICRAR) and the International Space Centre (ISC), The University of Western Australia, M468, 35 Stirling Highway, Crawley, WA 6009, Australia

⁸ ARC Centre of Excellence for All Sky Astrophysics in 3 Dimensions (ASTRO 3D), Level 2, 11 Lancaster Place, Canberra Airport, ACT 2609, Australia

⁹ Department of Physics and Astronomy, University of Missouri, Columbia, MO 65211, USA

¹⁰ AURA for the European Space Agency (ESA), Space Telescope Science Institute, 3700 San Martin Drive, Baltimore, MD 21210, USA

¹¹ Space Telescope Science Institute, 3700 San Martin Drive, Baltimore, MD 21210, USA

¹² National Research Council of Canada, Herzberg Astronomy & Astrophysics Research Centre, 5071 West Saanich Road, Victoria, BC V9E 2E7, Canada

Received 2023 June 21; revised 2023 September 22; accepted 2023 October 2; published 2023 November 16

Abstract

We identify 71 distant stars in James Webb Space Telescope/NIRCam early release observations (ERO) images of the field of galaxy cluster SMACS J0723.3-7327 (SMACS 0723). Given the relatively small ($\sim 10^\circ$) angular separation between SMACS 0723 and the Large Magellanic Cloud (LMC), it is likely that these stars are associated with the LMC outskirts or the Leading Arm. This is further bolstered by a spectral energy distribution (SED) analysis, which suggests an excess of stars at a physical distance of 40–100 kpc, consistent with being associated with or located behind the Magellanic system. In particular, we find that the overall surface density of stars brighter than 27.0 mag in the field of SMACS 0723 is ~ 2.3 times that of stars in a blank field with similar Galactic latitude (the North Ecliptic Pole Time Domain Field), and that the density of stars in the SMACS 0723 field with SED-derived distances consistent with the Magellanic system is ~ 6.1 times larger than that of the blank field. The candidate stars at these distances are consistent with a stellar population at the same distance modulus with $[\text{Fe}/\text{H}] = -1.0$ and an age of ~ 5.0 Gyr. On the assumption that all of the 71 stars are associated with the LMC, then the stellar density of the LMC at the location of the SMACS 0723 field is ~ 740 stars kpc^{-3} , which helps trace the density of stars in the LMC outskirts.

Unified Astronomy Thesaurus concepts: [Galactic archaeology \(2178\)](#); [Stellar spectral types \(2051\)](#); [James Webb Space Telescope \(2291\)](#)

Supporting material: machine-readable table

1. Introduction

The Magellanic clouds are the most massive satellite galaxies of the Milky Way (MW; McConnachie 2012), so they can provide a uniquely detailed look at how massive satellite galaxies and MW-like host galaxies interact. Also, they are the only nearby satellites of the MW that are not devoid of gas (Putman et al. 2021). Those two seem connected—most satellite galaxies of this mass are star forming (Wheeler et al. 2014), but how tidal and ram pressure stripping processes affect galaxies like the Large Magellanic Cloud (LMC) and Small Magellanic Cloud (SMC) in orbit around the MW is not fully understood. A more detailed view of the structure and dynamics of the Magellanic clouds can help improve our understanding of the interaction between the clouds and the MW, and in turn these environmental processes. A detailed

orbital history of the Magellanic clouds can provide clues about the properties (mass and concentration) of the MW (e.g., Santos-Santos et al. 2021).

The Magellanic system (see D’Onghia & Fox 2016 for a review) consists of the LMC, the SMC, the Magellanic Bridge (between the LMC and SMC; Hindman et al. 1963), the Magellanic Stream (behind the LMC and SMC; Mathewson et al. 1974), and the Leading Arm (ahead of the LMC and SMC; Putman et al. 1998). The Leading Arm was first identified by Putman et al. (1998) in the HI Parkes All-Sky Survey as a thin region leading the LMC-SMC system at higher velocities. Lu et al. (1998) further connected the Leading Arm to the LMC and SMC by finding similarities to LMC and SMC S/Fe abundance ratios in a high-velocity cloud in the Leading Arm.

As a key rung in the distance ladder (Riess et al. 2022), the stellar populations of the LMC and SMC have been studied in detail. The distance modulus to the LMC has been measured to be 18.48 ± 0.05 (based on a combination of Cepheids, luminous red variables, RR Lyrae stars, red clump stars, and

eclipsing binaries), which corresponds to a distance between 48.5 and 50.8 kpc (Walker 2011; Pietrzyński et al. 2019; Riess et al. 2019). The SMC is around 10 kpc farther away, measured with similar techniques (Graczyk et al. 2013). The velocity distribution of HI clouds in the Leading Arm is consistent with a distance between 40 and 70 kpc (Venzmer et al. 2012). Some simulations of the Magellanic Stream predict that it is ~ 20 kpc from the Sun at its closest point, with a stellar component that is even closer (Lucchini et al. 2021).

The Leading Arm spans around 70° in the sky, has an inclination against the sky of $\sim 13.6^\circ$ (almost face on), and spans around 52 kpc (Brüns et al. 2005; Venzmer et al. 2012). Most observations of the Leading Arm are of HI gas, of which Venzmer et al. (2012) estimated a lower limit HI mass of $3.8 \times 10^7 M_\odot$, compared to $4.4 \times 10^8 M_\odot$ for the LMC and $4.0 \times 10^8 M_\odot$ for the SMC (Brüns et al. 2005). However, the overall properties of the Leading Arm are not as well studied as the clouds themselves.

The formation of the Leading Arm must involve tidal forces, although additional forces such as ram pressure stripping may have been involved in its formation (Nidever et al. 2008). At the same time, the Magellanic Stream could have formed due to ram pressure stripping (Meurer et al. 1985; Moore & Davis 1994) or by blowout from supernovae (Nidever et al. 2008). With ram pressure forces and blowout, a stellar component is not expected, while tidal models do predict a stellar component for the Leading Arm. Initial searches did not detect a stellar component of the Magellanic Stream (Putman et al. 2003; Nidever et al. 2008). However, Casetti-Dinescu et al. (2014) observed six young stars in the Leading Arm, between 10 and 40 kpc from the Sun, as well as one low radial velocity O6V star at ~ 40 kpc, providing evidence for recent star formation within the Leading Arm. Thus, the properties of the Leading Arm can be inferred from the stellar populations that are observed within it.

In addition to the Magellanic Stream and Leading Arm, the Magellanic outskirts are of great interest (e.g., Saha et al. 2010; Mackey et al. 2016, 2018; Nidever et al. 2017, 2019; Choi et al. 2018a, 2018b; Cullinane et al. 2020; Drlica-Wagner et al. 2021; Petersen et al. 2022). Studying the outskirts of the LMC can reveal the extent of Magellanic stellar populations in the sky as well as the star formation history of these regions (Nidever et al. 2017). Furthermore, surveys around the LMC can help identify dwarf galaxies bound to the LMC/SMC (Drlica-Wagner et al. 2016), stellar streams neighboring the clouds (Drlica-Wagner et al. 2021), and faint star clusters at large physical distances (Nidever et al. 2017).

Kinematic information, combined with chemical information, from the periphery of the clouds can constrain the evolutionary history of the LMC-SMC-MW system (Muñoz et al. 2023). Cullinane et al. (2022) used data from fields between $\sim 8^\circ$ and $\sim 11^\circ$ from the center of the LMC to constrain the kinematics of the LMC-SMC-MW system. They also observed a mean metallicity of $[\text{Fe}/\text{H}] \approx -1$ across the 17 LMC fields analyzed. Petersen et al. (2022) showed that the LMC halo extends out to 30° from the LMC center.

The James Webb Space Telescope (JWST) provides a unique opportunity to study the stellar component of the LMC outskirts and Magellanic Leading Arm. The high resolution of the JWST, combined with its ability to search for faint stars out to $m \sim 27$ mag (with signal-to-noise ratio, $S/N \approx 35$ for a 3000 s exposure in F200W; e.g., Figures 6–8 of Windhorst

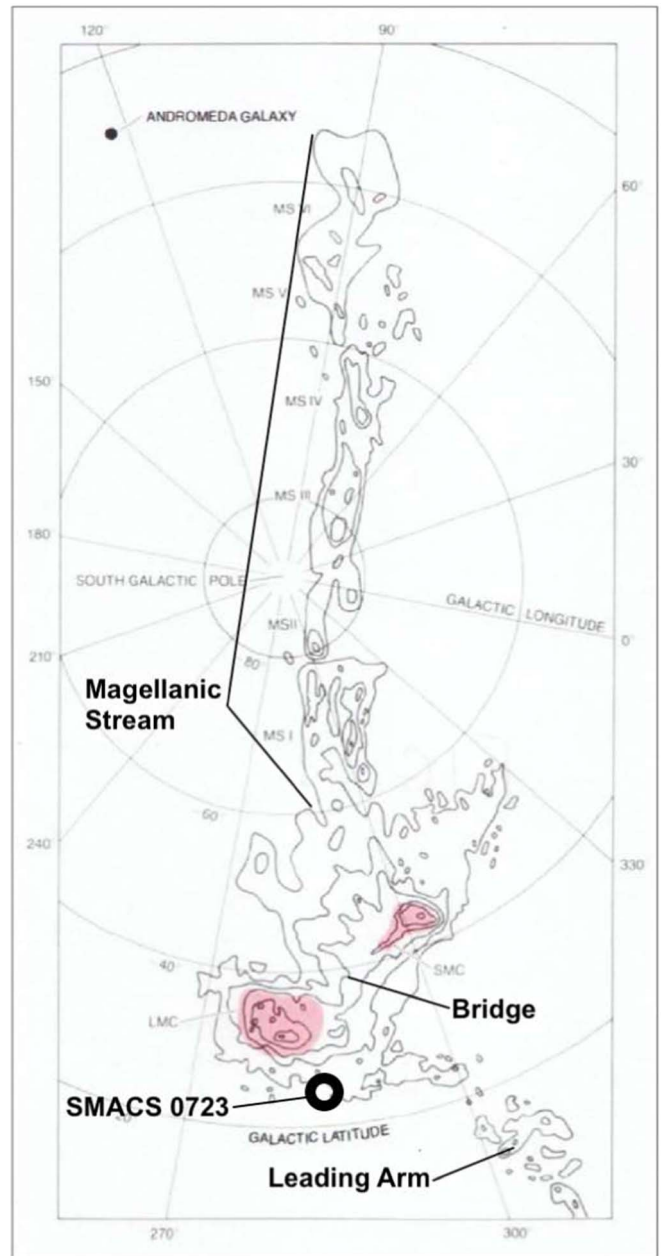


Figure 1. Map of HI in the LMC-SMC system, in Galactic coordinates, showing the location of the field of SMACS 0723. The SMACS 0723 field is near the Leading Arm and is part of the LMC outskirts, only $\sim 10^\circ$ from the center of the LMC. This image is reproduced from Figure 3 of Mathewson (2012), with explicit permission from the editors of JAHH, with additional annotations showing the location of the Magellanic Bridge, Leading Arm, Magellanic Stream, and SMACS 0723 field. The outermost contours represent 10^{19} atoms cm^{-2} .

et al. 2023), allows us to search for late-type stellar populations within the Magellanic system.

In this paper, we use JWST observations of the SMACS J0723.3-7327 galaxy cluster to search for stars that belong to the Magellanic system. Such stars likely belong to the Magellanic outskirts, given that the field of SMACS J0723.3-7327 is located between two of the 17 fields observed by Cullinane et al. (2022; see Figure 1 for a diagram of its location relative to the Magellanic system). In Section 2, we describe the observations, the data-reduction process, and the source-detection methods. In Section 3, we describe the spectral

energy distribution (SED)-fitting methods used. In Section 4, we describe the results from the SED fitting and the associated uncertainties. Table 1 in Section 5 provides a list of 71 candidate stars that are within the expected distance range of the Magellanic system, and we compare these candidate stars to theoretical isochrones to estimate metallicities and ages. We conclude with a summary and prospects for future studies in Section 6. We express all magnitudes in the AB system (Oke & Gunn 1983) unless otherwise noted.

2. Observations

2.1. Early Release Observations and PEARLS Observations

The primary JWST data used in this study are NIRCam images of the SMACS J0723.3-7327 (hereafter SMACS 0723) field from the JWST early release observations (ERO 2736, PI: K. Pontoppidan). For comparison, we also use NIRCam images of three fields from the Prime Extragalactic Areas for Reionization and Lensing Science (hereafter PEARLS) survey (GTO 1176, PI: R. Windhorst; GTO 2738, PI: R. Windhorst & H. Hammel): the North Ecliptic Pole Time Domain Field (hereafter NEPTDF), the IRAC Dark Field (hereafter IDF), and the MACS J0416.1-2403 (hereafter MACS 0416) galaxy cluster. We refer the reader to Pontoppidan et al. (2022) for more details on the SMACS 0723 observations and Windhorst et al. (2023) for details about the PEARLS program.

The PEARLS images used cover the first two spokes of the NEPTDF, the first two epochs of the IDF, and all three epochs of MACS 0416. The NEPTDF and IDF are medium-deep blank fields in the North Ecliptic Pole region and MACS 0416 is a galaxy cluster at $z=0.4$ (Caminha et al. 2017). SMACS 0723 is a galaxy cluster at $z=0.39$ (e.g., Repp & Ebeling 2018; Coe et al. 2019; Pascale et al. 2022; Mahler et al. 2023). SMACS 0723 and the North Ecliptic Pole have roughly similar angular separations from the Galactic bulge of 75° and $95^\circ 8'$, respectively.¹³

The SMACS 0723 field was observed on 2022 June 7 in the F090W, F150W, F200W, F277W, F356W, and F444W NIRCam filters, with an exposure time of 7537 s in each band. These observations reach a 5σ AB magnitude limit of ~ 29.5 mag for point sources with a $0''.08$ aperture radius according to the JWST exposure time calculator. Module B of NIRCam is centered on the galaxy cluster, while module A is the noncluster module. The coordinates of SMACS 0723 are R.A. = $07^{\text{h}} 23^{\text{m}} 19^{\text{s}}.5$, decl. = $-73^\circ 27' 15''.6$.

Spoke 1 of the NEPTDF was observed with the JWST/NIRCam on 2022 August 26 and 2022 September 14 with an observation time of 2920 s in the F090W, F115W, F410M, and F444W bands, and an observation time of 3350 s in the F150W, F200W, F277W, and F356W bands for each pointing. Spoke 2 was observed on 2022 November 26–27 with the same exposure parameters. The NEPTDF has coordinates of R.A. = $17^{\text{h}} 22^{\text{m}} 47^{\text{s}}.9$, decl. = $+65^\circ 49' 21''.5$ (Windhorst et al. 2023).

Epoch 1 of the IDF was observed by NIRCam on 2022 July 8 with an observation time of 3157 s in the F150W, F200W, F356W, and F444W filters; epoch 2 was observed on 2023 January 6 with the same exposure parameters. The coordinates of the IDF are R.A. = $17^{\text{h}} 40^{\text{m}} 8^{\text{s}}.5$, decl. = $+68^\circ 58' 27''.0$ (Windhorst et al. 2023).

MACS 0416 was observed by NIRCam for three epochs with, for each epoch, an observation time of 3779 s in F090W, F115W, F410M, and F444W, and an observation time of 2920 s in F150W, F200W, F277W, and F356W. Epoch 1 was taken on 2022 October 7, epoch 2 on 2022 December 29, and epoch 3 on 2023 February 10. The coordinates of MACS 0416 are R.A. = $4^{\text{h}} 16^{\text{m}} 8^{\text{s}}.9$, decl. = $-24^\circ 4' 28''.7$ (Windhorst et al. 2023). The NEPTDF, IDF, and MACS 0416 reach approximately 29.0 mag at 5σ for point sources in F200W with an aperture radius of $0''.08$ (Windhorst et al. 2023).

In addition to JWST NIRCam data of the SMACS 0723 cluster, the MACS 0416 cluster, the NEPTDF, and the IDF, we also use public Hubble Space Telescope (HST) data of SMACS 0723 from the Reionization Lensing Cluster Survey (RELICS) program (GO 14096, PI: D. Coe). RELICS provides HST images and catalogs, of which we use the combined Advanced Camera for Surveys (ACS) and Wide Field Camera 3/Infrared (IR) catalog (Cerny et al. 2018; Salmon et al. 2020), with magnitudes in the F435W, F606W, F814W, F105W, F125W, F140W, and F160W filters. These observations have 5σ point source AB magnitude limits between 26.0 and 27.6 mag (Coe et al. 2019), and provide useful information at optical wavelengths for objects detected in the JWST data. For stars, these shorter wavelengths are critical for distinguishing between the hottest spectral types. These data are used in Section 3.3 as consistency checks, but are not used in the final analysis.

We matched the positions of stars and galaxies in the NIRCam images to those of the RELICS images. Given the 1σ astrometric residuals of ~ 148 mas between the two datasets, we found only one star to have exhibited possible proper motion of more than 3σ and therefore concluded that proper motion is not significant between the HST and JWST observations.

2.2. Data Reduction

All NIRCam uncal data were retrieved from the Mikulski Archive for Space Telescopes (MAST). For all stages of the JWST calibration pipeline, data from SMACS 0723, the first epoch of the NEPTDF, the IDF, and MACS 0416 were reduced using version 1.7.2 of the pipeline and `pmap_0995`. Version 1.8.4 and `pmap_1017` were used for epoch 2 of the NEPTDF/IDF. Finally, version 1.8.4 and `pmap_1027` were used to reduce epoch 2 and `pmap_1041` was used for epoch 3 of MACS 0416. The difference between the various pipeline versions was minimal as no major NIRCam reference file updates were released between `pmap_0995` and 1041. The data were then processed through stage 1 (`detectorlpipe-line`) of the JWST calibration pipeline, with a snowball flagging step performed before the jump detection step. Snowballs are caused by intense cosmic rays and are dealt with by expanding the data quality flags around such cosmic rays. C. Willott’s `dosnowballflags.py` algorithm was used to subtract snowballs.¹⁴

Next, wisps templates, which were constructed by CNAW from all publicly available NIRCam short-wavelength images, were subtracted from the NRCA3, NRCA4, NRCB3, and NRCB4 detectors for the F150W and F200W filter exposures (see Robotham et al. 2023 for an alternative method of removing wisps). Wisps are also present in F090W and F115W

¹³ The Galactic coordinates for SMACS 0723 and the NEPTDF are $l = 285^\circ 0'$, $b = -23^\circ 76'$ and $l = 95^\circ 8'$, $b = 33^\circ 6'$, respectively.

¹⁴ <https://github.com/chriswillott/jwst>

Table 1
Candidate LMC Stars Identified with Star–Galaxy Separation and Fit with IRTF Spectral Templates

ID	R.A. (deg)	Decl. (deg)	Photometry ^a						Properties		
			F090W (mag)	F150W (mag)	F200W (mag)	F277W (mag)	F356W (mag)	F444W (mag)	Type	χ^2_{red}	μ^b (mag)
1	110.86216700	−73.47061220	24.77	24.33	24.53	25.24	25.49	25.82	K7V	0.66	18.1 ^{+0.3} _{−0.3}
2	110.85557140	−73.47091030	24.95	24.69	24.97	25.58	26.05	26.56	K3V	0.66	19.0 ^{+0.3} _{−0.3}
3	110.71958260	−73.49692810	25.05	24.82	25.03	25.67	26.16	26.50	K3V	0.48	19.1 ^{+0.3} _{−0.3}
4	110.91536500	−73.45760250	26.30	25.84	26.04	26.78	26.89	27.34	K7V	0.89	19.4 ^{+0.4} _{−1.2}
5	110.67205510	−73.50673290	26.63	26.24	26.26	26.70	27.31	27.31	M1V	0.81	18.7 ^{+0.5} _{−1.0}
6	110.70759900	−73.49949690	26.50	25.99	26.16	26.69	27.21	27.55	M0V	0.27	19.2 ^{+0.5} _{−0.7}
7	110.67496690	−73.50461890	25.96	25.68	25.89	26.54	26.99	27.46	K3V	0.19	19.9 ^{+0.3} _{−0.3}
8	110.66512020	−73.50600780	26.55	26.06	26.24	26.79	27.15	27.29	M3V	0.38	18.3 ^{+0.7} _{−0.7}
9	110.70289650	−73.49699630	25.90	25.62	25.84	26.37	26.86	27.11	K3V	0.33	19.8 ^{+0.3} _{−0.4}
10	110.68002770	−73.50094110	24.80	24.62	24.87	25.52	26.08	26.39	K2V	0.52	19.3 ^{+0.3} _{−0.3}
11	110.89040420	−73.45783110	26.02	25.52	25.64	26.25	26.63	27.08	M0.5V	0.30	18.6 ^{+0.4} _{−0.7}
12	110.84920430	−73.46677800	23.09	23.07	23.39	24.00	24.48	24.91	G3Va	0.18	18.1 ^{+1.5} _{−0.4}
13	110.86553090	−73.46272980	25.87	25.63	25.89	26.46	26.82	27.26	K3V	0.36	19.9 ^{+0.3} _{−0.3}
14	110.72000470	−73.49268410	25.59	25.15	25.32	25.84	26.24	26.62	M0V	0.24	18.2 ^{+0.6} _{−0.6}
15	110.66805300	−73.50092820	22.86	22.99	23.36	24.04	24.57	24.94	G6.5V	0.30	18.8 ^{+0.3} _{−0.5}
16	110.72784760	−73.48935170	26.17	25.77	25.96	26.51	26.95	27.29	K7V	0.06	19.5 ^{+0.3} _{−0.3}
17	110.76571260	−73.48077720	25.91	25.47	25.67	26.11	26.55	26.84	M1V	0.35	18.2 ^{+0.7} _{−0.9}
18	110.87489520	−73.45841050	25.19	25.08	25.36	25.99	26.40	26.88	K2V	0.03	19.8 ^{+0.3} _{−0.3}
19	110.73000210	−73.48620160	25.43	25.02	25.28	25.83	26.36	26.71	K7V	0.48	19.0 ^{+0.4} _{−0.3}
20	110.71625750	−73.48854100	26.05	25.60	25.79	26.36	26.69	26.99	M0V	0.47	18.6 ^{+0.7} _{−1.0}
21	110.72057470	−73.48737060	26.53	26.16	26.36	26.91	27.34	27.80	K7V	0.10	19.9 ^{+0.4} _{−0.3}
22	110.80594110	−73.46958100	25.72	25.34	25.58	26.18	26.53	26.90	K7V	0.43	19.2 ^{+0.5} _{−0.3}
23	110.68128930	−73.49252790	25.04	24.91	25.19	25.76	26.25	26.52	K2V	0.38	19.5 ^{+0.3} _{−0.3}
24	110.80106310	−73.46821900	24.89	24.63	24.82	25.40	25.87	26.26	K3V	0.09	18.8 ^{+0.3} _{−0.3}
25	110.75536650	−73.47725180	25.74	25.40	25.60	26.06	26.45	26.75	K7V	0.69	19.0 ^{+0.4} _{−0.8}
26	110.68680600	−73.49055430	26.78	26.26	26.46	26.97	27.35	28.14	M0V	0.82	19.8 ^{+0.4} _{−0.4}
27	110.64580220	−73.49817030	24.37	24.30	24.52	25.16	25.70	25.98	K2V	0.25	19.0 ^{+0.3} _{−0.3}
28	110.82877260	−73.46026270	22.95	23.07	23.44	24.08	24.55	24.97	G1V	0.17	18.9 ^{+0.3} _{−0.5}
29	110.72096780	−73.48176010	25.78	25.40	25.60	26.10	26.52	26.87	K7V	0.21	19.1 ^{+0.3} _{−0.3}
30	110.67001300	−73.49191860	26.37	25.94	26.09	26.62	27.05	27.44	M0V	0.12	19.3 ^{+0.4} _{−0.8}
31	110.64265760	−73.49445510	23.86	23.67	24.01	24.65	25.20	25.56	K2V	0.50	18.4 ^{+0.3} _{−0.3}
32	110.81476720	−73.45898890	23.29	23.33	23.65	24.26	24.72	25.14	K0V	0.13	18.5 ^{+1.4} _{−0.3}
33	110.72384130	−73.47836710	26.10	25.76	25.97	26.51	26.98	27.40	K3V	0.30	19.8 ^{+0.4} _{−0.4}
34	110.63281260	−73.49283500	25.68	25.16	25.40	25.96	26.50	26.94	M0V	0.67	18.9 ^{+0.3} _{−0.3}
35	110.72055620	−73.47503090	24.00	23.91	24.23	24.81	25.33	25.72	K1V	0.10	18.7 ^{+0.3} _{−0.3}
36	110.66272890	−73.48596090	25.92	25.65	25.85	26.44	26.96	27.41	K5V	0.06	19.8 ^{+0.3} _{−0.3}
37	110.65067740	−73.49085180	26.12	25.79	25.96	26.52	27.01	27.31	K7V	0.34	19.7 ^{+0.5} _{−0.3}
38	110.84558040	−73.44554930	24.30	24.28	24.61	25.22	25.65	26.09	G3Va	0.17	19.3 ^{+1.6} _{−0.4}
39	110.80421890	−73.45313020	24.13	24.09	24.44	24.98	25.48	25.86	G3Va	0.23	19.1 ^{+0.4} _{−0.4}
40	110.67477770	−73.47867250	25.45	25.14	25.37	25.95	26.45	26.82	K3V	0.08	19.4 ^{+0.3} _{−0.3}
41	110.63467750	−73.48880260	24.35	24.07	24.36	24.93	25.44	25.81	K3V	0.37	18.3 ^{+0.3} _{−0.3}
42	110.79796380	−73.45281710	26.56	25.94	26.08	26.73	27.12	27.56	M1.5V	0.33	19.1 ^{+0.3} _{−0.7}
43	110.64595860	−73.48242080	22.72	22.87	23.24	23.86	24.43	24.81	G1V	0.15	18.7 ^{+0.3} _{−0.5}
44	110.83642120	−73.44363830	25.95	25.57	25.77	26.27	26.58	27.00	K7V	0.47	19.1 ^{+0.4} _{−1.1}
45	110.76016130	−73.45909700	25.50	25.19	25.45	25.99	26.40	26.89	K3V	0.07	19.4 ^{+0.3} _{−0.4}
46	110.72820980	−73.46594990	24.27	24.38	24.58	25.10	25.70	26.12	G3Va	0.54	19.4 ^{+1.5} _{−0.4}
47	110.78956710	−73.45340770	26.71	26.31	26.46	27.05	27.36	27.61	K7V	0.58	19.2 ^{+0.8} _{−1.1}
48	110.83748180	−73.44288410	25.02	24.67	24.87	25.44	25.91	26.31	K7V	0.28	18.6 ^{+0.4} _{−0.3}
49	110.65875080	−73.47794840	26.18	25.71	25.84	26.43	26.88	27.12	M1V	0.36	18.7 ^{+0.6} _{−0.6}
50	110.78230860	−73.45339920	26.37	25.93	26.00	26.69	27.03	27.62	M0V	0.39	19.4 ^{+0.3} _{−0.3}
51	110.78782340	−73.45101940	23.53	23.51	23.82	24.41	24.94	25.31	G3Va	0.18	18.5 ^{+0.4} _{−0.4}
52	110.85693660	−73.43664670	26.00	25.70	25.91	26.42	26.84	27.40	K3V	0.20	19.9 ^{+0.3} _{−0.4}
53	110.66720140	−73.47507180	25.12	24.92	25.20	25.63	26.17	26.57	K3V	0.84	19.2 ^{+0.3} _{−0.4}
54	110.81224460	−73.44403790	23.88	23.77	24.05	24.59	25.04	25.46	K2V	0.26	18.4 ^{+0.3} _{−0.3}
55	110.66261310	−73.47706440	24.46	24.33	24.63	25.23	25.77	26.14	K2V	0.07	19.0 ^{+0.3} _{−0.3}
56	110.78046660	−73.45030070	26.49	26.12	26.31	26.82	27.17	27.61	K7V	0.25	19.8 ^{+0.3} _{−0.4}

Table 1
(Continued)

ID	R.A. (deg)	Decl. (deg)	Photometry ^a						Properties		
			F090W (mag)	F150W (mag)	F200W (mag)	F277W (mag)	F356W (mag)	F444W (mag)	Type	χ^2_{red}	μ^b (mag)
57	110.76385480	-73.45338740	25.74	25.40	25.62	26.17	26.64	27.07	K3V	0.27	19.5 ^{+0.4} _{-0.4}
58	110.79180220	-73.44578380	23.77	23.71	24.06	24.67	25.13	25.57	G3Va	0.37	18.7 ^{+0.4} _{-0.4}
59	110.77367240	-73.44919120	25.65	25.25	25.47	26.12	26.56	27.03	K7V	0.67	19.3 ^{+0.4} _{-0.4}
60	110.77943010	-73.44784300	26.23	25.88	26.04	26.55	26.93	27.25	K7V	0.50	19.4 ^{+0.4} _{-0.8}
61	110.62570660	-73.47884900	22.68	22.76	23.14	23.70	24.24	24.64	G2V	0.13	18.2 ^{+0.6} _{-0.3}
62	110.84937560	-73.43260770	22.94	23.00	23.39	24.10	24.47	24.88	G2V	0.83	18.7 ^{+0.4} _{-0.5}
63	110.75095580	-73.45261390	25.81	25.45	25.65	26.19	26.60	27.07	K7V	0.17	19.2 ^{+0.4} _{-0.3}
64	110.83870650	-73.43454150	25.64	25.39	25.56	26.09	26.52	26.96	K3V	0.33	19.5 ^{+0.3} _{-0.4}
65	110.67197890	-73.46799340	26.70	26.22	26.38	26.86	27.31	27.90	M0V	0.36	19.6 ^{+0.4} _{-0.6}
66	110.61303870	-73.47875580	24.38	24.03	24.27	24.85	25.37	25.77	K3V	0.22	18.3 ^{+0.3} _{-0.4}
67	110.79838860	-73.43960650	26.59	26.07	26.24	26.82	27.23	27.61	M0V	0.37	19.1 ^{+0.5} _{-0.7}
68	110.64934660	-73.46977780	25.55	25.21	25.47	26.01	26.55	26.97	K3V	0.16	19.4 ^{+0.3} _{-0.3}
69	110.81135150	-73.43491940	25.24	24.98	25.16	25.76	26.18	26.65	K3V	0.11	19.2 ^{+0.3} _{-0.3}
70	110.65634220	-73.46544270	25.81	25.33	25.53	26.04	26.42	26.78	M1V	0.31	18.1 ^{+0.7} _{-0.8}
71	110.61594180	-73.47252690	25.59	25.32	25.55	26.07	26.55	26.83	K3V	0.30	19.5 ^{+0.3} _{-0.4}

Notes.

^a As discussed in Section 2.3, reported photometry was measured on point-spread function (PSF)-matched NIRCcam mosaics. Apparent magnitude uncertainties are not displayed because they are very small ($\lesssim 0.01$ mag). All reported magnitudes use the AB system.

^b From the SED fits using templates from the IRTF Spectral Library (Cushing et al. 2005; Rayner et al. 2009). Distance moduli are calculated individually for each filter and averaged where the lower uncertainty is the 16th percentile, the reported value is the 50th percentile, and the upper uncertainty is the 84th percentile of the cumulative probability distribution for a given star. The uncertainties are added in quadrature with an additional uncertainty of 0.25 mag due to SpeX flux calibration uncertainties. Only stars with $18 \leq \mu \leq 20$ mag are taken as candidates.

(This table is available in machine-readable form.)

in the NEP TDF, but there is presently not enough public data that contain these wisps to make a high S/N template.

Following the wisp subtraction, the rate files were reduced with the default stage 2 pipeline (`calwebbimage2`). After this, a correction for $1/f$ noise was applied using the ProFound package (Robotham et al. 2018), which also performed sky subtraction. Both an overall sky level and a sky gradient were fit with ProFound and subtracted from each image (see Windhorst et al. 2023 for more details). Finally, the data were astrometrically aligned and drizzled to mosaics with a pixel size of $0''.03$ using the JWST stage 3 pipeline (`calwebbimage3`). SMACS 0723 data were relatively aligned, whereas NEP TDF, IDF, and MACS 0416 data were aligned to Gaia Data Release 3 (DR3).

2.3. Photometry

We use `SourceExtractor` (Bertin & Arnouts 1996) for source detection in the NIRCcam images. First, a set of PSF-matched (to F444W) images is created. These are made by using `pypher` (Boucaud et al. 2016) to calculate the necessary convolution kernel to match each filter’s PSF to that of the F444W PSF, where the PSFs are simulated using `WebbPSF` (Perrin et al. 2012). This convolution results in all PSFs having approximately the same FWHM and shape. `SourceExtractor` is then run on the images in dual-image mode with F444W as the detection filter and with `DETECT_MINAREA = 9`, `DETECT_THRESH = 1.5`, and a 5×5 pixel Gaussian convolution kernel with a FWHM of three pixels. F444W is among the deepest of the images, and using it results in the greatest number of stars being found, so it is used as the detection image. The `MAG_AUTO` of each source is taken to be its observed magnitude.

To select stars from the object catalogs, we use similar methods to Windhorst et al. (2011). We require `MAG_AUTO < 27` and that `FWHM_IMAGE` lies within the stellar locus of the middle plot in Figure 2, i.e., the FWHM fell between $0''.14$ and $0''.18$ in all filters (widening for stars brighter than 20 mag). The magnitude requirement is used to avoid classifying small, faint galaxies as stars. An object is classified as a star if it fits these criteria in at least three NIRCcam filters.

3. SED Fitting

Near-IR SEDs are fit to the stars to estimate their distances and spectral types. To conduct the SED fitting, we use the framework of `EAZY` (Brammer et al. 2008) given its flexibility at conducting this analysis, though we emphasize that we use separate stellar SED templates rather than galaxy SED templates. To do this, the maximum redshift is set to $z = 0$ and the minimum filters used in the fitting is set to 4. Before fitting SEDs, the catalogs (other than the IDF, which is only used for star counts) are corrected for Galactic extinction ($A_V = 0.587$ mag for SMACS 0723, $A_V = 0.082$ mag for the NEP TDF, and $A_V = 0.101$ mag for MACS 0416). We apply the full value of A_V to better fit distant stars that have more Galactic dust in front of them. The A_V values are likely quite different between fields due to LMC dust in the field of SMACS 0723, although the correction only causes an adjustment of ~ 0.05 mag in F200W for SMACS 0723. The SMACS 0723 RELICS catalog has the same A_V correction by default. We use fluxes for the `EAZY` SED fitting.

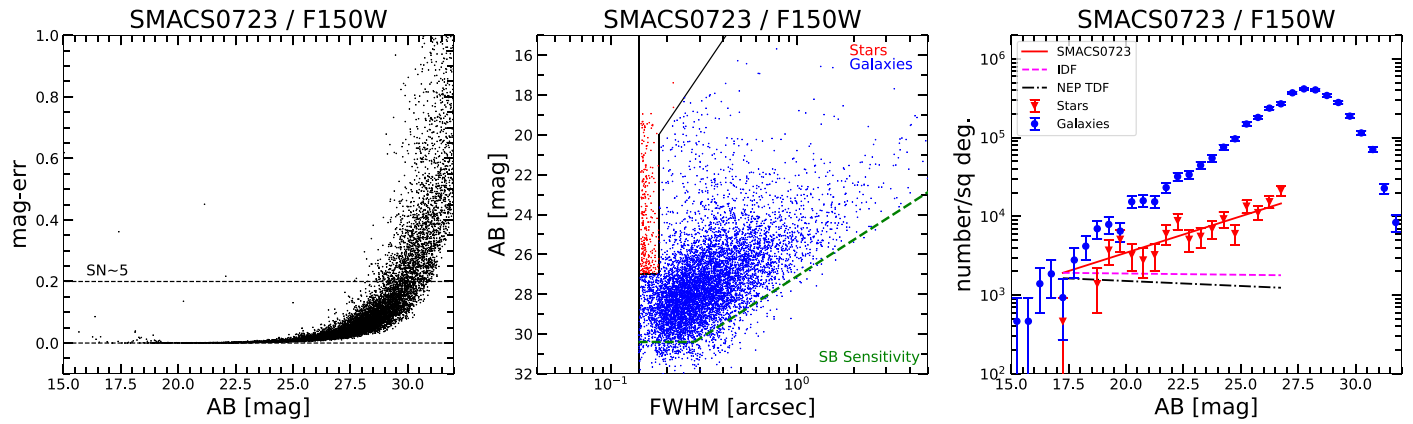


Figure 2. Left: SourceExtractor MAGERR_AUTO vs. MAG_AUTO for the F150W NIRCcam filter, with a horizontal dashed line establishing the uncertainty needed for a source to have a S/N of 5. Middle: MAG_AUTO vs. FWHM_IMAGE, with stars plotted in red based on the FWHM and magnitude separation criteria. The green dashed line shows the point source and surface brightness sensitivity limit for the corresponding image (for details, see Windhorst et al. 2023). Right: star (red) and galaxy (blue) counts per square degree vs. MAG_AUTO. Best-fit lines of the star counts are plotted for SMACS 0723, the NEP TDF, and the IDF for comparison. The slope of the best-fit line for SMACS 0723 stars is greater than that of the other fields—there is an excess of faint stars.

3.1. Template Construction

Instead of default galaxy SED templates, we use stellar SED templates from the SpeX IRTF Spectral Library from Rayner et al. (2009) and Cushing et al. (2005). The SpeX library covers wavelengths of 0.8–5.0 μm , with templates for stars with MW abundances, cooler in temperature than type A.¹⁵ We only fit main sequence stars because they account for most stars in the LMC field. If we assume there are 25,000 asymptotic giant branch (AGB) stars per 16 deg^2 , as in Wiśniewski et al. (2011), then there could be around three AGB stars in the NIRCcam SMACS 0723 data. This is insignificant compared to the number of total stars observed, and since we are focusing on the overall trend in star distances, these stars can safely be ignored.

We then use `pysynphot` (STScI Development Team 2013) to compute the apparent magnitude in every NIRCcam filter for each stellar SED template. The Gaia parallax of each SpeX star is then used to determine its absolute magnitude in each NIRCcam filter (Gaia Collaboration et al. 2016, 2022; Babusiaux et al. 2022). Since the spectral type for main sequence stars roughly correlates with their absolute magnitudes, the absolute magnitude of each SpeX star can be estimated given its parallax-based distance and its apparent magnitude.

3.2. Bayesian Probabilities

When fitting stellar SEDs with EAZY, the code is run once for each individual template, the template is fit to every star and spectral type, χ^2 , and observed/template SEDs are recorded. All stars with a best-fit $\chi^2_{\text{red}} > 2$ are removed from the final catalog. This cut removes 21 objects from the SMACS 0723 catalog. Most high χ^2 objects are likely either not main-sequence stars or have questionable photometry.

To provide an estimate of the distance moduli, μ , of the stars in SMACS 0723, we measure the posterior probability distributions of the distance modulus for each star. To do this, we use the output from EAZY, which provides the fitting

parameters for every star for each stellar SED template. Bayes’ theorem is then used:

$$P(\text{Template}|\text{Fluxes}) = \frac{P(\text{Fluxes}|\text{Template})P(\text{Template})}{\sum_i P(\text{Fluxes}|\text{Template}_i)}, \quad (1)$$

where each term is a probability. The measured fluxes in each NIRCcam filter for a given star are the “Fluxes” and the spectra for a given spectral type (SpeX star) is the “Template.” Equation (1) solves $P(\text{Template}|\text{Fluxes})$ (the posterior probability), which is the probability that a star fits a particular SpeX SED template, assuming that the fluxes are accurate. $P(\text{Fluxes}|\text{Template})$ is the probability that the fluxes are correct, assuming that the star fits a particular SpeX SED template (which corresponds to a spectral type), and $P(\text{Template})$ is the probability of a random star fitting the SpeX SED template (the prior). We assume a constant prior probability model (changing this to reflect the MW initial mass function (IMF) has almost no effect on the results) on absolute magnitude, turning Equation (1) into the following:

$$P(\text{Template}|\text{Fluxes}) = \frac{P(\text{Fluxes}|\text{Template})}{\sum_i P(\text{Fluxes}|\text{Template}_i)}. \quad (2)$$

We calculate $P(\text{Fluxes}|\text{Template})$ as the product of Gaussian distributions (one per filter) centered at each predicted flux, with a standard deviation equal to EAZY `err_full` (which includes photometric uncertainty and template uncertainty), evaluated at the measured flux. The posterior probability for each template fitting a given star is equal to the probability that the template fits the star divided by the sum of the probabilities over all of the templates. This posterior probability distribution (as a function of spectral type, which each has a corresponding absolute magnitude) is then calculated for all stars in all filters and is converted from spectral types to absolute magnitudes. The probability distributions are then converted to distance moduli by subtracting the distribution from each filter’s apparent magnitude. Therefore, each distribution gives the probability that a given star is fit with a given distance

¹⁵ Templates for F2V, F3V, F4V, F5V, F7V, F8V, F9.5V, G0V, G1V, G2V, G3Va, G5V, G6.5V, G8V, K0V, K1V, K2V, K3V, K5V, K7V, M0V, M0.5V, M1V, M1.5V, M2.5V, M3V, M3.5V, M4V, M5V, M6V, M6.5V, M7V, M8V, M9V, M9.5V, L1, L3, L3.5, and L5 stars are used from http://irtfweb.ifa.hawaii.edu/~spex/IRTF_Spectral_Library/.

modulus. These probability distributions are then linearly interpolated and all six to eight of them (six to eight NIRCcam filters) are summed together for each star. These probability density functions are normalized to an area of one, and are used to calculate the lower bound, median, and upper bound of the distance modulus for each star. This is done by measuring the 16th, 50th, and 84th percentile in the cumulative probability distribution, respectively. Thus, the reported uncertainties correspond to 1σ uncertainty. Measuring the probability densities of each star allows for a more complete assessment of uncertainties, reported in Table 1.

3.3. HST Checks

To confirm the SED fits from the SpeX library of stellar SEDs, we use stellar SED templates from the optical library from Pickles (1998). For stars in the field of SMACS 0723 that have HST data available (there are 90 of them), the optical HST data (F435W, F606W, F814W, F105W, F125W, F140W, and F160W) and short-wavelength NIRCcam data (F090W, F150W, and F200W) are fit with EAZY by the Pickles (1998) templates (the templates cover 0.12–2.50 μm in wavelength) for a variety of main sequence stars.¹⁶ The Pearson correlation coefficient (r) was calculated between the shared templates for the two spectral libraries over their shared wavelengths, and all templates except for the M5V ($r \approx 0.76$) template agree to $r \gtrsim 0.97$. However, the M5V template is the last template available from the Pickles (1998) library, so this is to be expected.

Since the Pickles (1998) templates are normalized and combine multiple stars for the creation of each template, we assume each template has the same absolute magnitude as the SpeX star with the same spectral type. The absolute magnitudes fit by the two libraries have the greatest agreement at $M_{F090W} \lesssim 7$ mag, where the standard deviation of their difference is ~ 0.35 mag. This limited range of agreement is to be expected because the SpeX library offers a greater variety of late-type stellar SED templates compared to the Pickles (1998) library. Since the SpeX library leads to similar results as the Pickles (1998) library, covers more near-IR wavelengths, and has a wider variety of M-star templates, it is reasonable to use the SpeX library with all of the SMACS 0723, NEP TDF, and MACS 0416 photometry.

4. Magellanic Star Candidate Identification

4.1. The Distance Modulus

We consider two ways of estimating the distribution of distance moduli of stars in the SMACS 0723 field. First, we consider the distribution of distance estimates of each star (using the 50th percentile of the distance modulus probability density function, PDF). Alternatively, all of the probability distributions of each star can be added up to form one probability distribution for each field as a whole. Figure 3 shows the distribution of the 50th percentile distance moduli for each field. The ratio of the distributions, shown in the middle plot, shows a clear surplus of stars in the field of SMACS 0723 at $18 \lesssim \mu \lesssim 20$ mag, which corresponds to a distance between ~ 39.8 and ~ 100.0 kpc. We refer to the stars

in this range of distances as stellar candidates; however, the properties of each individual star are more uncertain compared to the population as a whole. Additionally, some candidate stars could be part of the MW halo since the JWST photometry does not have the spectral resolution to detect precise metallicity differences between individual stars. The integrated surface density between these distance moduli is $\sim 50,500$ stars deg^{-2} in the SMACS 0723 field compared to ~ 8200 stars deg^{-2} in the NEP TDF. This means that the field of SMACS 0723 has ~ 6.1 times as many stars per square degree as the NEP TDF between 39.8 and 100 kpc, compared to an overall ratio of ~ 2.3 and a ratio at all distances other than $18 \leq \mu \leq 20$ mag of ~ 1.9 .

Overall, the probability distribution for the SMACS 0723 field has ~ 7600 more stars $\text{deg}^{-2} \text{mag}^{-1}$ than the NEP TDF. However, between 39.8 and 100 kpc the difference is $\sim 21,100$ stars $\text{deg}^{-2} \text{mag}^{-1}$. Figure 3 shows the difference in 50th percentile star counts between the SMACS 0723 field and the two other fields in the bottom plot. The field of SMACS 0723 has a clear excess between 39.8 and 100 kpc, whereas the NEP TDF and MACS 0416 field have a minor excess relative to the SMACS 0723 field at closer distances. Hence, there is a significant surplus of stars (15.3σ compared to the NEP TDF, 7.2σ compared to the field of MACS 0416) in the field of SMACS 0723 at this distance.

The range of distances found in this paper is different compared to Casetti-Dinescu et al. (2014), who observed early-type stars at a distance of up to ~ 40 kpc. The stars observed in this paper are farther than 40 kpc, likely because the field of SMACS 0723 is closer in the sky to the LMC than those in Casetti-Dinescu et al. (2014). The star candidates are expected to be closer to ~ 50 kpc because they are only $\sim 10^\circ$ from the LMC and the field of SMACS 0723 is near the line of nodes for the LMC's inclination (Cullinane et al. 2022), unlike the stars in Casetti-Dinescu et al. (2014), which were farther stars in the Leading Arm.

4.2. Contamination

Since SMACS 0723 is a galaxy cluster, an obvious source of contamination would be dwarf galaxies or globular clusters within the galaxy cluster. We would expect foreground LMC stars to be distributed randomly throughout the SMACS 0723 images, and not concentrated in the NIRCcam module that contains the SMACS 0723 cluster center. As a test, we counted the numbers of stellar candidates in the NIRCcam module centered on the cluster (32 stellar candidates) and offset from the SMACS 0723 cluster (39 stellar candidates), obtaining numbers that are less concentrated toward the cluster center. Figure 4 shows the number of candidates as a function of X-coordinate. Since the mosaics are not rotated to have north at the top, the X-coordinate is equivalent to the lengthwise distance along the NIRCcam field of view. As expected, there is a dip in star counts close to the module gap. There is an excess of candidate stars near the brightest cluster galaxy (BCG), but the noncluster module has a similar spike in stars elsewhere, so we conclude that contamination in this catalog is unlikely. The centroid of LMC candidates for each NIRCcam module is $\lesssim 250$ pixels from the center of each module. Thus, the candidates are not skewed in a certain direction and are randomly distributed as expected.

¹⁶ Available templates include those of O5V, O9V, B0V, B1V, B3V, B6V, B8V, A0V, A2V, A3V, A5V, F0V, F2V, F5V, F8V, G0V, G2V, G5V, G8V, K0V, K2V, K5V, K7V, M0V, M4V, and M5V stars from <https://archive.stsci.edu/hlsps/reference-atlases/cdbs/grid/pickles/>.

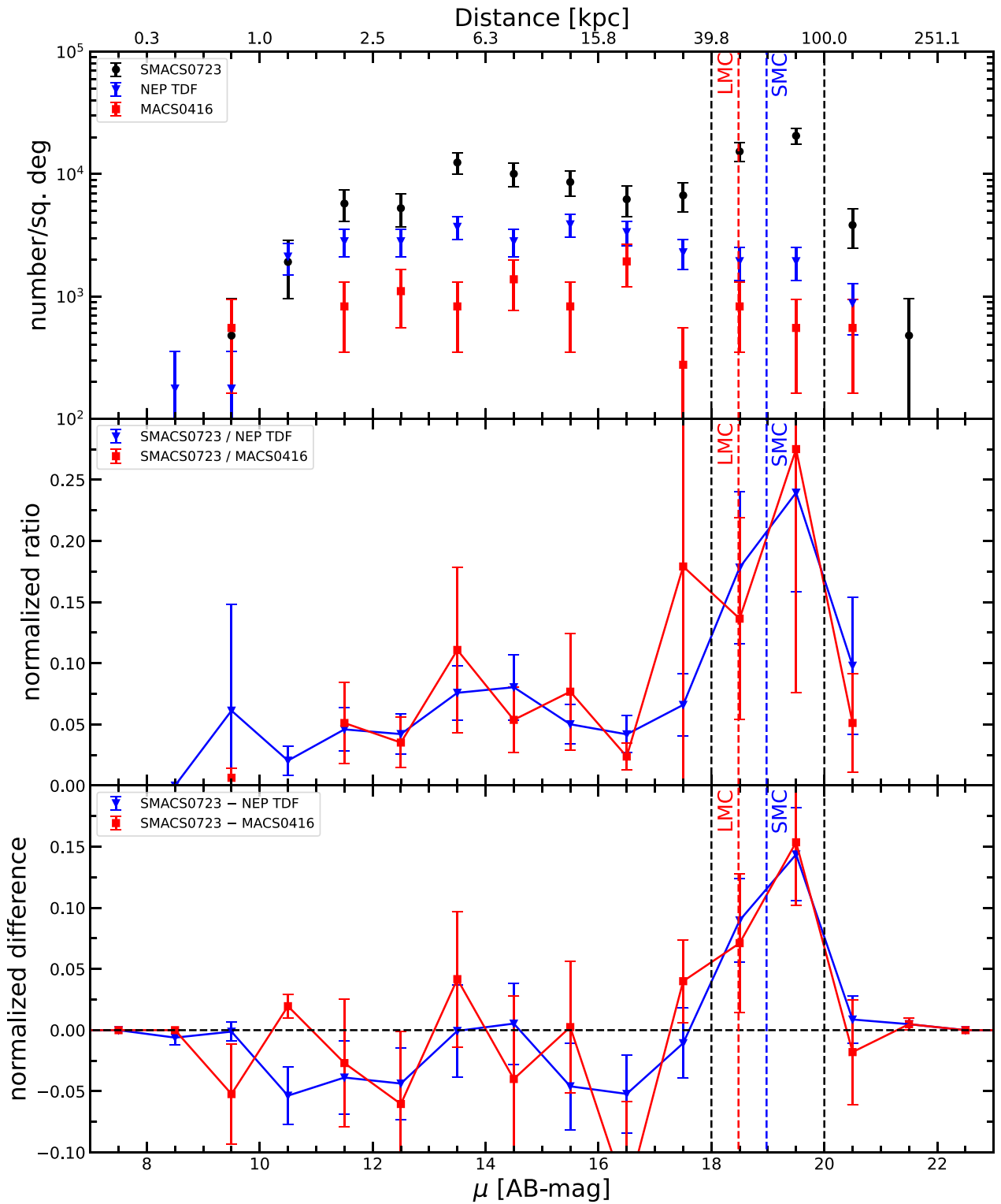


Figure 3. Distribution of distance moduli, μ (calculated from the 50th percentile in the distance modulus PDF) for stars in the SMACS 0723, NEP TDF, and MACS 0416 fields. Top: binned distance moduli for stars in each field. Middle: ratio of stars found at each distance in SMACS 0723 compared to the NEP TDF and MACS 0416, normalized to have a sum of 1. Bottom: difference in probability density between SMACS 0723 and the NEP TDF/MACS 0416 fields, where the data from each field are normalized to have a sum of 1 (resulting in a difference of zero between fields). The vertical black dashed lines at a distance modulus of 18 and 20 mag show the ranges of candidates taken, the vertical red dashed lines shows the distance to the LMC, and the vertical blue dashed lines show the distance to the SMC.

In addition to the spatial distribution of candidate stars in the field of SMACS 0723, the inclusion of MACS 0416 (which has approximately the same redshift at $z = 0.4$ as SMACS 0723 at

$z = 0.38$) data further corroborates that there is little to no contamination. In particular, Figure 3 shows that there is no excess of stars in the field of MACS 0416 at $18 \leq \mu \leq 20$ mag.

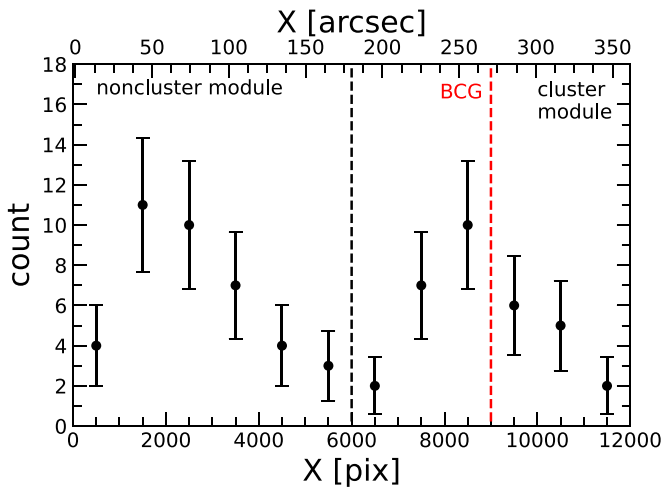


Figure 4. Histogram of X -positions of candidate stars in the SMACS 0723 mosaics. Error bars show \sqrt{N} uncertainties. The noncluster module is on the left of the vertical black dashed line and the cluster module is on the right, with the position of the brightest cluster galaxy shown as a vertical red dashed line. No significant excess of candidate LMC stars around the BCG is detected.

Thus, the excess in point sources at $18 \leq \mu \leq 20$ mag is not caused by contamination from the SMACS 0723 galaxy cluster.

4.3. Uncertainty in μ

There are various contributions in the uncertainty budget of the calculated distance moduli, including photometric uncertainties, SpeX calibration uncertainties, and SED fit uncertainties, which we account for. Uncertainties that are unaccounted for include distance-dependent dust extinction as well as metallicity differences between the stars observed and the EAZY templates used.

Photometric uncertainties in the NIRCcam data and the SpeX calibration only contribute $\lesssim 3\%$ uncertainties to the distance moduli. This was verified using Monte Carlo methods: the observed magnitudes were resampled based on their `SourceExtractor` uncertainties 1000 times for each star, the 1000 probability distributions for each star were averaged together, and the 50th percentile in the PDF of distance moduli was recalculated to be $\lesssim 3\%$ of the distance modulus calculated with only the observed magnitudes. The calibration for the IRTF spectral library is within a few percent (Rayner et al. 2009).

For a conservative estimate on uncertainty in the SED templates, the 2MASS photometry typically has uncertainties of $\lesssim 0.25$ mag, so we add this number in quadrature to the final upper and lower uncertainties. The uncertainty in parallax for each of the SpeX stars used is $\lesssim 0.01$ mag, and is therefore negligible. Finally, the SED fit uncertainties are described in Section 3.2 and generally have the greatest contribution to the overall uncertainty in μ . Thus, the 2MASS photometric uncertainty and the SED fit uncertainties are used to calculate the final uncertainties in μ , reported in Table 1.

4.4. Gaia Stars

A Gaia DR3 (Gaia Collaboration et al. 2016, 2022; Babusiaux et al. 2022) query¹⁷ was performed in each of the

fields studied in this paper to check if any of the detected stars had measured parallaxes. A handful of JWST stars from each field have parallaxes and proper motions, but the uncertainties are large enough to render them unhelpful. As a separate check, a Gaia DR3 query with a larger area was undertaken around the field of SMACS 0723 and the NEP TDF to check for an excess of stars at the distance of the LMC. However, due to the shallower depth of Gaia, no significant excess of low-parallax stars nor stars with small proper motion characteristic of the LMC was found. Thus, Gaia data alone are not enough to detect an excess of stars around the field of SMACS 0723 at the distance of the LMC.

5. Magellanic Star Candidate Properties

5.1. Age and Metallicity Estimates

We now set out to estimate the approximate ages and metallicities of the LMC candidate stars. When selecting star candidates that are part of the Magellanic system, we required that $18 \leq \mu \leq 20$ mag and $\chi_{\text{red}}^2 < 1$. This range of distances allows for the detection of nearby stars in the Leading Arm (possibly around 40 kpc) as well as farther stars in the Magellanic outskirts closer to 50 kpc. The smaller χ_{red}^2 value selects only the candidates that fit their stellar template the best. These LMC stellar candidates are presented in Table 1.

Figure 5 shows all of the stars on color–magnitude diagrams, with isochrones corresponding to stellar populations between $\mu = 18$ mag and $\mu = 20$ mag. The isochrones are created using MESA Isochrones and Stellar Tracks data (Paxton et al. 2011, 2013, 2015; Choi et al. 2016; Dotter 2016). The isochrones assume $[\text{Fe}/\text{H}] = -1.0$ and $v/v_{\text{crit}} = 0.4$ rotation rates. We also generate isochrones of $[\text{Fe}/\text{H}] = 0.0$ to represent MW stars. Most of the candidate stars (colored shapes) fall in the range of the isochrones, reflecting that the candidates form their own stellar population. The other detected stars (black dots) that fall around the isochrones generally have a distance modulus close to that of the LMC, but outside the range of distance moduli used to select candidates.

The characteristics of the isochrones reflect the metallicity of this stellar component in the LMC. The implied metallicities seem to be consistent with $[\text{Fe}/\text{H}] = -1.0$. This metallicity is consistent with that of stars observed in the LMC outskirts (Cullinane et al. 2022). Many candidates have colors and magnitudes that are not consistent with having $[\text{Fe}/\text{H}] = 0.0$, so are not likely to be MW stars. Some other candidates presented could be MW stars, but that information could only be distinguished via precise metallicity or proper motion measurements. The stars that are almost considered candidates, with $\mu \lesssim 18$ mag or $\mu \gtrsim 20$ mag, could also be LMC stars, but we cannot be certain of this since the difference between the SMACS 0723 field and the NEP TDF at that physical distance is not significant.

Figure 5 also shows a color–color diagram with the candidate stars as colored shapes and the other detected stars as black dots. In general, the candidates are closer to the lower left (hotter) than the bulk of observed stars; many noncandidate stars are closer to the upper right (type M). Additionally, the isochrone of 10 Gyr (with $[\text{Fe}/\text{H}] = -1.0$) shows that at least a few candidates are inconsistent with the ages of MW halo stars.

Of all 204 stars identified in the field of SMACS 0723, only two are fit as type F stars. These two stars have relatively blue

¹⁷ The Gaia DR3 catalog can be queried at <https://gea.esac.esa.int/archive/>.

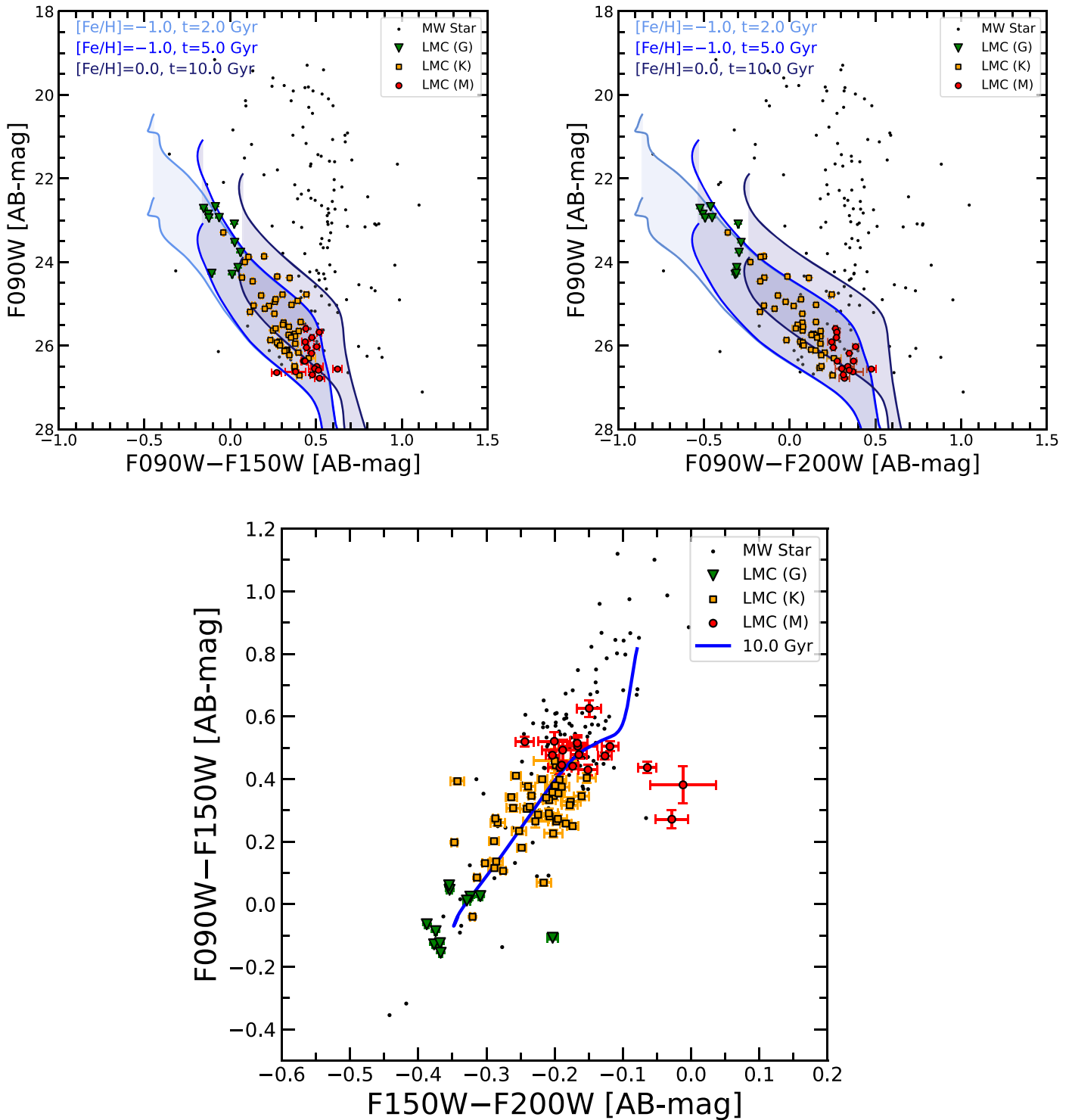


Figure 5. Top: color–magnitude diagrams including the 71 candidate stars (with colored shapes corresponding to different spectral types) and the rest of the detected stars (black dots). Plotted on them are shaded isochrones of various ages and metallicities for distance moduli between 18 and 20 mag. Bottom: color–color diagram with the 71 candidate stars as well as an isochrone of $t = 10.0$ Gyr and $[\text{Fe}/\text{H}] = -1.0$. A few candidates typed as G stars must be younger than this age.

colors, and can be seen as black dots in the bottom-left corner of the color–color diagram in Figure 5. These stars are the bluest two stars in the color–magnitude diagrams in Figure 5. Both stars have HST data available. The first of the two type F stars was fit as F9.5V with $\mu = 20.2^{+0.8}_{-0.3}$ mag using the SpeX templates and G6.5V with $\mu = 19.9^{+0.3}_{-0.3}$ mag using the Pickles (1998) templates. The second star was fit as type F5V with both

libraries, and had $\mu = 18.0^{+0.4}_{-0.7}$ mag using the SpeX templates and $\mu = 18.5^{+0.3}_{-0.6}$ mag using the Pickles (1998) templates. Thus, both stars are slightly outside the criteria used for selecting Magellanic system candidates. However, it is still possible that these stars are part of the LMC outskirts. If this is the case, then there could be recent star formation within the LMC outskirts from <5.0 Gyr ago.

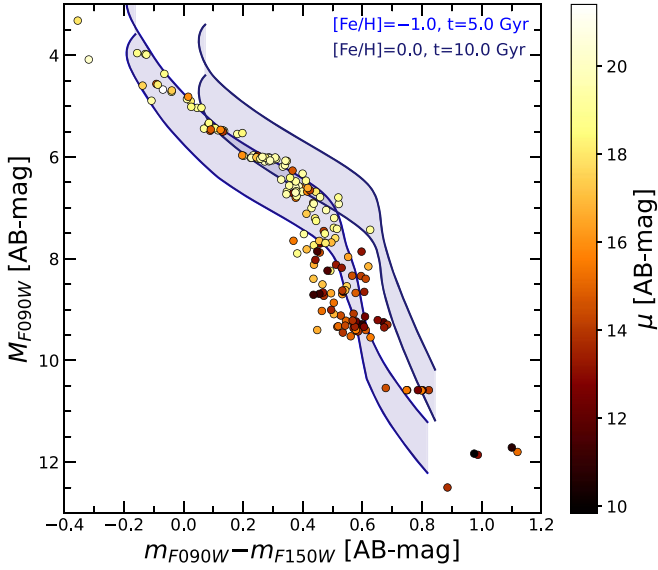


Figure 6. H-R diagram of all stars observed in the field of SMACS 0723. Distance modulus (μ) is indicated by the color scheme, and isochrones are plotted to indicate the expected positions of an old MW stellar population and a younger LMC population.

5.2. Absolute Magnitudes and Masses

We now use the measured absolute magnitudes of the stars in the field of SMACS 0723 to evaluate the properties of each stellar population (MW and LMC) as well as estimate stellar masses. Figure 6 shows a Hertzsprung–Russell (H-R) diagram for the stars observed in this study. Bluer stars tend to be fit by either $[\text{Fe}/\text{H}] = -1.0$ or $[\text{Fe}/\text{H}] = 0$. However, redder stars are better fit by the $[\text{Fe}/\text{H}] = -1.0$ model.

We now use the measured absolute magnitudes to compare our observed stellar luminosity function (LF) to that in Figure 6 of Just et al. (2015). Figure 7 shows the LF for the set of MW stars, the set of LMC stars, and the Just et al. (2015) results. The data are normalized to have a sum of 1 for stars brighter than the completeness limits. Just et al. (2015) plot nearly all stars in the 20 pc sphere around the Sun, whereas the field of SMACS 0723 is a single pointing outside the MW disk. The LF observed for the LMC candidates is ~ 2 mag brighter than that of the closer MW stars ($\mu < 18$ mag). Additionally, the LF observed for the MW stars matches up better with the Just et al. (2015) LF, although it is incomplete for $M_{K_s} \gtrsim 9$ mag.

Using the absolute magnitudes derived for each star, we then estimate stellar masses. To do this, we measure the K_s absolute magnitude for each SpeX template using `pysynphot` (STScI Development Team 2013). This allows us to use the mass relations in Henry & McCarthy (1993). The results of this analysis are plotted in Figure 8. We compare the observed IMFs to the Salpeter (1955) and Chabrier (2003) MW IMF, plotted in purple, as well as the Sirianni et al. (2000) LMC IMF, plotted in green. The results are not complete for lower mass stars, but the MW star masses ($\mu < 18$ mag) show agreement for $-0.6 \leq \log(M/M_\odot) \leq 0.2$. The LMC stellar masses ($18 < \mu < 20$ mag), on the other hand, are more biased toward higher mass stars and do not fit the MW IMF well. The LMC IMF is not complete for low masses and so does not overlap with our data.

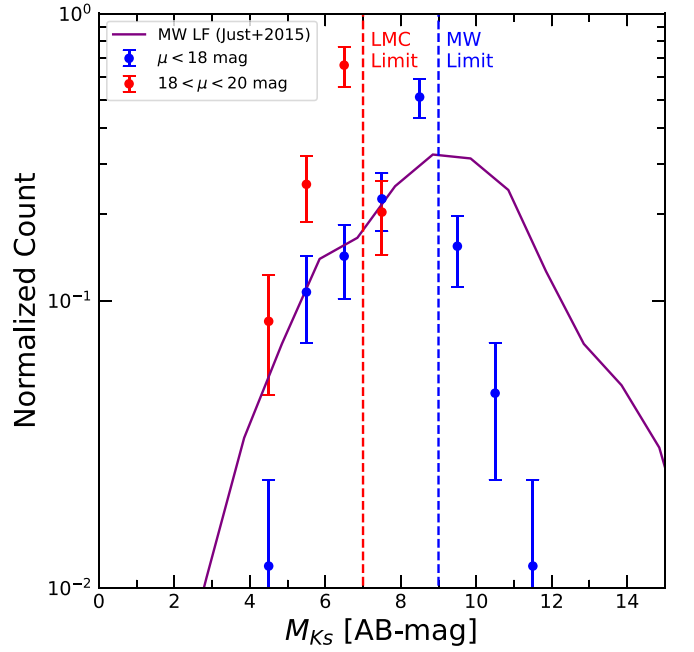


Figure 7. Histogram of absolute magnitudes (in the 2MASS K_s band pass) for both the LMC candidate stars (in red) and the remaining MW stars (in blue). The MW luminosity function measured in Just et al. (2015) is plotted in purple. Dashed lines indicate the incompleteness limit of our sample (due to the magnitude cutoff of $m < 27$ mag and the distance cutoffs for each population).

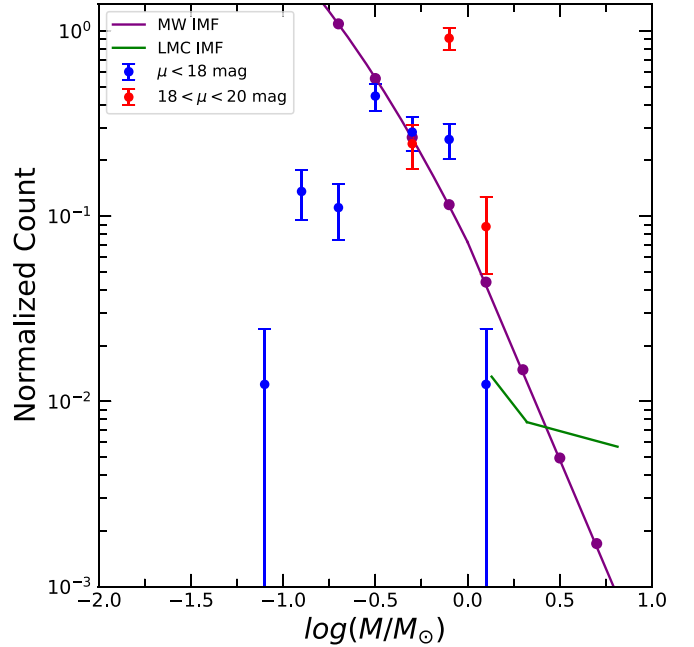


Figure 8. Histogram of masses observed in each stellar population (MW, blue: $\mu < 18$ mag; LMC, red: $18 < \mu < 20$ mag). The MW IMF is plotted in purple using the Salpeter (1955) IMF for $\log(M/M_\odot) \geq 0$ and the Chabrier (2003) IMF for $\log(M/M_\odot) \leq 0$. The IMF observed in Sirianni et al. (2000) for LMC star clusters is plotted in green for $0.13 \leq \log(M/M_\odot) \leq 0.81$. Graphs are normalized to a sum of 1 for masses greater than the completeness limits. Any mass bins with counts less than 10^{-2} have zero stars in them and are not plotted.

5.3. Stellar Density

Taking the areal coverage of SMACS 0723 to be $\sim 0.002 \text{ deg}^2$, our 71 candidates would lead to a stellar density of $\sim 34,000 \text{ deg}^{-2}$. This corresponds to a spatial density at a

distance of 50 kpc (between 40 and 100 kpc from the Sun) of 740 stars kpc^{-3} . This spatial density will further help models constrain the orbital history of the Magellanic system around the MW. In particular, measuring the stellar density profile of the LMC can help reveal faint features of the LMC other than the primary elliptical profile (Massana et al. 2020). With shallower data, the surface brightness profile of the LMC was not detected beyond Galactocentric radii of $\sim 8^\circ$ (Massana et al. 2020); deeper data at farther radii, such as with the field of SMACS 0723, can reveal a more complete LMC profile. Compared to Cullinane et al. (2022), we observe many more faint stars, since the angular density of Gaia stars around this area of the LMC outskirts (around the field of SMACS 0723 and two Cullinane et al. 2022 fields) is only ~ 45 stars/deg $^{-2}$. The ages observed are inconsistent with $t = 10$ Gyr because there are a few type G stars (plotted as stars and triangles in Figure 5) that are likely relatively young. This suggests that the group of stars observed has a similar dynamical age as the body of the LMC.

The expected number of main sequence turnoff (MSTO) stars at an angular distance of 10° from the LMC center is around 600 stars deg $^{-2}$ (Nidever et al. 2019). Since our data goes deeper, it is difficult to directly compare our results with other studies. However, if we take the number of G stars (since the MSTO in Nidever et al. 2019 go to ~ 9 Gyr) observed in the field of SMACS 0723 at near LMC distance, we find ~ 5300 stars deg $^{-2}$. If instead we consider stars with $2.5 \text{ mag} \leq M_{F090W} \leq 4.5 \text{ mag}$, we find a stellar density of ~ 1900 stars deg $^{-2}$. These stellar densities are somewhat different due to using different methods to select stars. This could mean that there are more LMC stars in the direction of SMACS 0723, or that the comparison is inexact.

6. Conclusion

We observe a total of 71 candidate stars that are between 39.8 and 100 kpc from the Sun, according to their SED-derived distance moduli. These stars are in a field that is $\sim 10^\circ$ or ~ 9 kpc from the LMC. We present information about these candidates in Table 1. The candidate stars could be in the outskirts of the LMC or part of the MW halo. They could also be part of the Leading Arm, but the distances are too uncertain to separate the Leading Arm from the LMC outskirts. The stars lie around isochrones of this distance with $[\text{Fe}/\text{H}] = -1.0$, which is the expected metallicity for stars in the LMC outskirts (Cullinane et al. 2022).

While our identification of a stellar overdensity is highly significant, the association of any individual object to the Magellanic system, as well as the exact distances/spectral types of individual objects, are more uncertain. Spectroscopy of these faint and crowded objects requires JWST to further constrain their stellar types, distances, and dynamics, allowing for a more complete picture of this interesting system.

Acknowledgments

We thank Ian Smail for helpful suggestions regarding the source-detection methods. We also thank Steven Willner and the referee for helpful suggestions that improved the submitted manuscript. J.S. acknowledges support from an undergraduate Arizona NASA Space Grant, Cooperative Agreement 80NSSC20M0041. R.A.W., S.H.C., and R.A.J. acknowledge support from NASA JWST Interdisciplinary Scientist grants

NAG5-12460, NNX14AN10G and 80NSSC18K0200 from GSFC. C.J.C. and N.J.A. acknowledge support from the European Research Council (ERC) Advanced Investigator Grant EPOCHS (788113). M.A.M. acknowledges the support of a National Research Council of Canada Plaskett Fellowship, and the Australian Research Council Centre of Excellence for All Sky Astrophysics in 3 Dimensions (ASTRO 3D), through project number CE17010001. C.N.A.W. acknowledges funding from the JWST/NIRCam contract NASS-0215 to the University of Arizona. We also acknowledge the indigenous peoples of Arizona, including the Akimel O’odham (Pima) and Pee Posh (Maricopa) Indian Communities, whose care and keeping of the land has enabled us to be at ASU’s Tempe campus in the Salt River Valley, where much of our work was conducted. This work is based on observations made with the NASA/ESA/CSA James Webb Space Telescope. The data were obtained from the Mikulski Archive for Space Telescopes (MAST) at the Space Telescope Science Institute, which is operated by the Association of Universities for Research in Astronomy, Inc., under NASA contract NAS 5-03127 for JWST. These observations are associated with JWST programs 1176, 2736, and 2738. All of the JWST data used in this paper can be found on doi:10.17909/b7hf-he53. This work is based on observations taken by the RELICS Treasury Program (Coe 2016, GO 14096) with the NASA/ESA HST, which is operated by the Association of Universities for Research in Astronomy, Inc., under NASA contract NAS5-26555. This work has made use of data from the European Space Agency (ESA) mission Gaia (<https://www.cosmos.esa.int/gaia>), processed by the Gaia Data Processing and Analysis Consortium (DPAC, <https://www.cosmos.esa.int/web/gaia/dpac/consortium>). Funding for the DPAC has been provided by national institutions, in particular the institutions participating in the Gaia Multilateral Agreement. We also acknowledge the JWST ERO team responsible for providing these products.¹⁸

Facilities: HST, JWST, MAST.

Software: Astropy (Astropy Collaboration et al. 2013, 2018, 2022); EAZY (Brammer et al. 2008); JWST Calibration Pipeline (Bushouse et al. 2022); Photutils (Bradley et al. 2022); ProFound (Robotham et al. 2018); Pypher (Boucaud et al. 2016); Pysynphot (STScI Development Team 2013); SourceExtractor (Bertin & Arnouts 1996); WebbPSF (Perrin et al. 2012).

ORCID iDs

Jake Summers  <https://orcid.org/0000-0002-7265-7920>
 Rogier A. Windhorst  <https://orcid.org/0000-0001-8156-6281>
 Seth H. Cohen  <https://orcid.org/0000-0003-3329-1337>
 Rolf A. Jansen  <https://orcid.org/0000-0003-1268-5230>
 Timothy Carleton  <https://orcid.org/0000-0001-6650-2853>
 Patrick S. Kamienieski  <https://orcid.org/0000-0001-9394-6732>
 Benne W. Holwerda  <https://orcid.org/0000-0002-4884-6756>
 Christopher J. Conselice  <https://orcid.org/0000-0003-1949-7638>
 Nathan J. Adams  <https://orcid.org/0000-0003-4875-6272>
 Brenda L. Frye  <https://orcid.org/0000-0003-1625-8009>

¹⁸ <https://www.stsci.edu/jwst/science-execution/approved-programs/webb-first-image-observations>

Jose M. Diego  <https://orcid.org/0000-0001-9065-3926>
 Christopher N. A. Willmer  <https://orcid.org/0000-0001-9262-9997>
 Rafael Ortiz, III  <https://orcid.org/0000-0002-6150-833X>
 Cheng Cheng  <https://orcid.org/0000-0003-0202-0534>
 Alex Pigarelli  <https://orcid.org/0000-0001-9369-6921>
 Aaron Robotham  <https://orcid.org/0000-0003-0429-3579>
 Jordan C. J. D'Silva  <https://orcid.org/0000-0002-9816-1931>
 Scott Tompkins  <https://orcid.org/0000-0001-9052-9837>
 Simon P. Driver  <https://orcid.org/0000-0001-9491-7327>
 Haojing Yan  <https://orcid.org/0000-0001-7592-7714>
 Dan Coe  <https://orcid.org/0000-0001-7410-7669>
 Norman Grogin  <https://orcid.org/0000-0001-9440-8872>
 Anton M. Koekemoer  <https://orcid.org/0000-0002-6610-2048>
 Madeline A. Marshall  <https://orcid.org/0000-0001-6434-7845>
 Nor Pirzkal  <https://orcid.org/0000-0003-3382-5941>
 Russell E. Ryan, Jr.  <https://orcid.org/0000-0003-0894-1588>

References

- Astropy Collaboration, Price-Whelan, A. M., Lim, P. L., et al. 2022, *ApJ*, **935**, 167
- Astropy Collaboration, Price-Whelan, A. M., Sipőcz, B. M., et al. 2018, *AJ*, **156**, 123
- Astropy Collaboration, Robitaille, T. P., Tollerud, E. J., et al. 2013, *A&A*, **558**, A33
- Babusiaux, C., Fabricius, C., Khanna, S., et al. 2023, *A&A*, **674**, A32
- Bertin, E., & Arnouts, S. 1996, *A&AS*, **117**, 393
- Boucaud, A., Bocchio, M., Abergel, A., et al. 2016, *A&A*, **596**, A63
- Bradley, L., Sipőcz, B., Robitaille, T., et al. 2022, *astropy/photutils*, v1.5.0, Zenodo, doi:[10.5281/zenodo.6825092](https://doi.org/10.5281/zenodo.6825092)
- Brammer, G. B., van Dokkum, P. G., & Coppi, P. 2008, *ApJ*, **686**, 1503
- Brüns, C., Kerp, J., Staveley-Smith, L., et al. 2005, *A&A*, **432**, 45
- Bushouse, H., Eisenhamer, J., Dencheva, N., et al. 2022, JWST Calibration Pipeline, v1.8.2, Zenodo, doi:[10.5281/zenodo.7229890](https://doi.org/10.5281/zenodo.7229890)
- Caminha, G. B., Grillo, C., Rosati, P., et al. 2017, *A&A*, **600**, A90
- Casetti-Dinescu, D. I., Moni Bidin, C., Girard, T. M., et al. 2014, *ApJL*, **784**, L37
- Cerny, C., Sharon, K., Andrade-Santos, F., et al. 2018, *ApJ*, **859**, 159
- Chabrier, G. 2003, *PASP*, **115**, 763
- Choi, J., Dotter, A., Conroy, C., et al. 2016, *ApJ*, **823**, 102
- Choi, Y., Nidever, D. L., Olsen, K., et al. 2018a, *ApJ*, **866**, 90
- Choi, Y., Nidever, D. L., Olsen, K., et al. 2018b, *ApJ*, **869**, 125
- Coe, D. 2016, Reionization Lensing Cluster Survey ("RELICS"), STScI/MAST, doi:[10.17909/T9SP45](https://doi.org/10.17909/T9SP45)
- Coe, D., Salmon, B., Bradač, M., et al. 2019, *ApJ*, **884**, 85
- Cullinane, L. R., Mackey, A. D., Da Costa, G. S., et al. 2020, *MNRAS*, **497**, 3055
- Cullinane, L. R., Mackey, A. D., Da Costa, G. S., et al. 2022, *MNRAS*, **512**, 4798
- Cushing, M. C., Rayner, J. T., & Vacca, W. D. 2005, *ApJ*, **623**, 1115
- D'Onghia, E., & Fox, A. J. 2016, *ARA&A*, **54**, 363
- Dotter, A. 2016, *ApJS*, **222**, 8
- Drlica-Wagner, A., Bechtol, K., Allam, S., et al. 2016, *ApJL*, **833**, L5
- Drlica-Wagner, A., Carlin, J. L., Nidever, D. L., et al. 2021, *ApJS*, **256**, 2
- Gaia Collaboration, Prusti, T., de Bruijne, J. H. J., et al. 2016, *A&A*, **595**, A1
- Gaia Collaboration, Vallenari, A., Brown, A. G. A., et al. 2023, *A&A*, **674**, A1
- Graczyk, D., Pietrzyński, G., Thompson, I. B., et al. 2013, *ApJ*, **780**, 59
- Henry, T. J., & McCarthy, D. W. J. 1993, *AJ*, **106**, 773
- Hindman, J. V., Kerr, F. J., & McGee, R. X. 1963, *AuJPh*, **16**, 570
- Just, A., Fuchs, B., Jahreiß, H., et al. 2015, *MNRAS*, **451**, 149
- Lu, L., Savage, B. D., Sembach, K. R., et al. 1998, *AJ*, **115**, 162
- Lucchini, S., D'Onghia, E., & Fox, A. J. 2021, *ApJL*, **921**, L36
- Mackey, A. D., Koposov, S. E., Erkal, D., et al. 2016, *MNRAS*, **459**, 239
- Mackey, D., Koposov, S., Da Costa, G., et al. 2018, *ApJL*, **858**, L21
- Mahler, G., Jauzac, M., Richard, J., et al. 2023, *ApJ*, **945**, 49
- Massana, P., Noël, N. E. D., Nidever, D. L., et al. 2020, *MNRAS*, **498**, 1034
- Mathewson, D. 2012, *JAHH*, **15**, 100
- Mathewson, D. S., Cleary, M. N., & Murray, J. D. 1974, *ApJ*, **190**, 291
- McConnachie, A. W. 2012, *AJ*, **144**, 4
- Meurer, G. R., Bicknell, G. V., & Gingold, R. A. 1985, *PASA*, **6**, 195
- Moore, B., & Davis, M. 1994, *MNRAS*, **270**, 209
- Muñoz, C., Monachesi, A., Nidever, D. L., et al. 2023, arXiv:2305.19460
- Nidever, D. L., Majewski, S. R., & Butler Burton, W. 2008, *ApJ*, **679**, 432
- Nidever, D. L., Olsen, K., Choi, Y., et al. 2019, *ApJ*, **874**, 118
- Nidever, D. L., Olsen, K., Walker, A. R., et al. 2017, *AJ*, **154**, 199
- Oke, J. B., & Gunn, J. E. 1983, *ApJ*, **266**, 713
- Pascale, M., Frye, B. L., Diego, J., et al. 2022, *ApJL*, **938**, L6
- Paxton, B., Bildsten, L., Dotter, A., et al. 2011, *ApJS*, **192**, 3
- Paxton, B., Cantiello, M., Arras, P., et al. 2013, *ApJS*, **208**, 4
- Paxton, B., Marchant, P., Schwab, J., et al. 2015, *ApJS*, **220**, 15
- Perrin, M. D., Soummer, R., Elliott, E. M., Lallo, M. D., & Sivaramakrishnan, A. 2012, *Proc. SPIE*, **8442**, 84423D
- Petersen, M. S., Peñarrubia, J., & Jones, E. 2022, *MNRAS*, **514**, 1266
- Pickles, A. J. 1998, *PASP*, **110**, 863
- Pietrzyński, G., Graczyk, D., Gallette, A., et al. 2019, *Natur*, **567**, 200
- Pontoppidan, K. M., Barrientes, J., Blome, C., et al. 2022, *ApJL*, **936**, L14
- Putman, M. E., Gibson, B. K., & Staveley-Smith, L. 1999, in *IAU Symp. 190, New Views of the Magellanic Clouds*, ed. Y.-H. Chu et al. (Cambridge: Cambridge Univ. Press)
- Putman, M. E., Staveley-Smith, L., Freeman, K. C., Gibson, B. K., & Barnes, D. G. 2003, *ApJ*, **586**, 170
- Putman, M. E., Zheng, Y., Price-Whelan, A. M., et al. 2021, *ApJ*, **913**, 53
- Rayner, J. T., Cushing, M. C., & Vacca, W. D. 2009, *ApJS*, **185**, 289
- Repp, A., & Ebeling, H. 2018, *MNRAS*, **479**, 844
- Riess, A. G., Casertano, S., Yuan, W., Macri, L. M., & Scolnic, D. 2019, *ApJ*, **876**, 85
- Riess, A. G., Yuan, W., Macri, L. M., et al. 2022, *ApJL*, **934**, L7
- Robotham, A. S. G., Davies, L. J. M., Driver, S. P., et al. 2018, *MNRAS*, **476**, 3137
- Robotham, A. S. G., D'Silva, J. C. J., Windhorst, R. A., et al. 2023, *PASP*, **135**, 085003
- Saha, A., Olszewski, E. W., Brondel, B., et al. 2010, *AJ*, **140**, 1719
- Salmon, B., Coe, D., Bradley, L., et al. 2020, *ApJ*, **889**, 189
- Salpeter, E. E. 1955, *ApJ*, **121**, 161
- Santos-Santos, I. M. E., Fattahi, A., Sales, L. V., & Navarro, J. F. 2021, *MNRAS*, **504**, 4551
- Sirianni, M., Nota, A., Leitherer, C., De Marchi, G., & Clampin, M. 2000, *ApJ*, **533**, 203
- STScI Development Team, 2013 pysynphot: Synthetic Photometry Software Package v2.0.0, Astrophysics Source Code Library, ascl:[1303.023](https://ascl.net/1303.023)
- Venzmer, M. S., Kerp, J., & Kalberla, P. M. W. 2012, *A&A*, **547**, A12
- Walker, A. R. 2011, *Ap&SS*, **341**, 43
- Wheeler, C., Phillips, J. I., Cooper, M. C., Boylan-Kolchin, M., & Bullock, J. S. 2014, *MNRAS*, **442**, 1396
- Windhorst, R. A., Cohen, S. H., Hathi, N. P., et al. 2011, *ApJS*, **193**, 27
- Windhorst, R. A., Cohen, S. H., Jansen, R. A., et al. 2023, *AJ*, **165**, 13
- Wiśniewski, M., Marquette, J. B., Beaulieu, J. P., et al. 2011, *A&A*, **530**, A8